Annals of Nuclear Energy 77 (2015) 212–222

Contents lists available at ScienceDirect

Annals of Nuclear Energy

journal homepage: www.elsevier.com/locate/anucene

Theory and analysis of accuracy for the method of characteristics direction probabilities with boundary averaging

Zhouyu Liu [a,*], Benjamin Collins [b], Brendan Kochunas [b], Thomas Downar [b], Yunlin Xu [b], Hongchun Wu [a]

[a] School of Nuclear Science and Technology, Xi'an Jiaotong University, No. 28 Xianning West Road, Xi'an, Shaanxi 710049, PR China
[b] Department of Nuclear Engineering and Radiological Sciences, University of Michigan, 2200 Bonisteel, Ann Arbor, MI 48109, USA

ARTICLE INFO

Article history:
Received 21 August 2014
Received in revised form 9 November 2014
Accepted 12 November 2014
Available online 1 December 2014

Keywords:
CDP
MOC
Boundary averaging

ABSTRACT

The method of characteristic direction probabilities (CDP) combines the benefits of the collision probability method (CPM) and the method of characteristics (MOC) for the solution of the integral form of the Botlzmann Transport Equation. By coupling only the fine regions traversed by the characteristic rays in a particular direction, the computational effort required to calculate the probability matrices and to solve the matrix system is considerably reduced compared to the CPM. Furthermore, boundary averaging is performed to reduce the storage and computation but the capability of dealing with complicated geometries is preserved since the same ray tracing information is used as in MOC. An analysis model for the outgoing angular flux is used to analyze a variety of outgoing angular flux averaging methods for the boundary and to justify the choice of optimize averaging strategy. The boundary average CDP method was then implemented in the Michigan PArallel Characteristic based Transport (MPACT) code to perform 2-D and 3-D transport calculations. The numerical results are given for different cases to show the effect of averaging on the outgoing angular flux, region scalar flux and the eigenvalue. Comparison of the results with the case with no averaging demonstrates that an angular dependent averaging strategy is possible for the CDP to improve its computational performance without compromising the achievable accuracy.

1. Introduction

Recently there has been considerable research into the development of direct, whole-core heterogeneous transport calculations which can provide pin resolved power distributions and improve the accuracy of LWR reactor physics simulations. There has been considerable progress that suggests whole-core transport calculations may become more widely used for practical LWR applications. The method of characteristics (MOC) has been used extensively in codes such as CASMO (Smith and Rhodes, 2000) to perform lattice calculations for LWR applications. Similar to the S_N methods, the MOC uses a set of discrete ordinates, but MOC is better suited to treat complicated geometries because it only requires an approximation on the spatial variation of the source and not on the flux itself along the tracing direction. However, the accurate discretization of the problem geometry can require a considerable number of characteristic rays, especially for the three dimensional spatial meshing required to represent very thin regions using burnable absorbers such as IFBA that coat the fuel pin. In such cases, the memory requirements for MOC can become prohibitive and limit the applicability of the method for practical problems. To overcome this problem modular ray tracing techniques have been developed in 2-D (Cho, 2005) and 3-D (Liu et al., 2011). In modular ray tracing, the ray data is only determined for a few geometrically unique sub-domains in the problem. This has been successfully implemented in several MOC codes (e.g., DeCART, MPACT, and CRX (Hong and Cho, 1998)). However the transport sweep still needs to be performed along all the characteristics lines for every direction, and this sweeping time can be computationally expensive.

The method of characteristic direction probabilities was first proposed for 2D problems by (Hong and Cho, 1999) and combined the desirable features of the MOC and the collision probability (CPM) (Sanchez, 1977). CPM has been widely used in lattice physics codes because it has the capability of treating the complicated geometries and is very efficient when dealing with small size problems. But this method has the drawback that the storage requirements and computing time depend on the square of the number of fine spatial regions in the problem. This is because the collision probability matrix couples all the fine mesh regions. Another drawback of CPM is that it cannot easily treat anisotropic

* Corresponding author.
E-mail addresses: liuzhouyu1985@hotmail.com (Z. Liu), bscollin@umich.edu (B. Collins), bkochuna@umich.edu (B. Kochunas), downar@umich.edu (T. Downar), yunlin@umich.edu (Y. Xu), hongchun@mail.xjtu.edu.cn (H. Wu).

http://dx.doi.org/10.1016/j.anucene.2014.11.016
0306-4549/

sources. The most significant difference between CPM and CDP is that in CDP only fine regions traversed by a characteristic line within a specified sub-domain are coupled which can significantly reduce the computational requirements. To overcome the drawback of CPM when dealing with big size problems, the interface current method (ICM) (Mohanakrishnan, 1981) was developed which couples the sub-domains with interface current of interface current moments, and within the domains the fine regions are coupled by the CPM. However, compared to the interface current method, CDP doesn't introduce the approximation at the interface of the subdomain and the anisotropic sources.

The standard method of 2-D and 3-D modular characteristics has been implemented in MPACT (Michigan PArallel Characteristics Transport code) as the fundamental discretization for the MOC transport kernels. As described in previous research, the method of modular characteristic direction probabilities (Liu et al., 2013) was extended for 3D transport calculations using the same ray tracing scheme as the MOC. However, boundary averaged ray tracing information is provided only for unique sub-domains which has the benefit of reducing the storage and data transfer for every sub-domain because of the reduced number of boundary conditions.

At the same time, the CDP is capable of providing the same accuracy as MOC if the unique boundary sub-domains are the same size as the MOC ray spacing. The only difference in the methods then would be that instead of performing the transport sweep ray by ray of the MOC, the CDP method obtains the outgoing angular flux and fine region flux by direct multiplication of a matrix which contains the collision and transmission probabilities with a vector which includes the incoming angular flux and the fine region source. The collision and transmission probabilities in the CDP are derived by integrating the traditional MOC equations along a characteristic line. So in principle, the method of characteristics direction probabilities is mathematically consistent with the conventional MOC if no averaging approximation at the sub-domain boundary is introduced. This has been confirmed by the previous work (Liu et al., 2013). The essential new feature provided by the boundary averaged CDP introduced here is the potential to introduce angular dependent averaging methods which could coarsen the boundary regions for particular angles, and thereby reduce the computational burden without compromising accuracy.

In the following section the basic equations of the MOC are provided along with the derivation of the CDP method. The third section describes the analysis model introduced to analyze the boundary outgoing angular flux and the boundary averaging scheme. Numerical results are shown in the subsequent section and the final section provides a summary and conclusions.

2. The method of characteristics direction probabilities

2.1. The method of characteristics

The classical method of characteristics for solving partial differential equations has been successfully applied to the Boltzmann Transport equation (BTE) and implemented in several reactor analysis codes. The group-wise form of the BTE for the system R with a boundary ∂R is given by

$$\Omega \cdot \nabla \varphi_g(\boldsymbol{r}, \boldsymbol{\Omega}) + \Sigma_{t,g} \varphi_g(\boldsymbol{r}, \boldsymbol{\Omega}) = Q_g(\boldsymbol{r}, \Omega) \tag{1}$$

and

$$Q_g(\boldsymbol{r}, \boldsymbol{\Omega}) = Q_{f,g}(\boldsymbol{r}) + Q^{iso}_{s,g}(\boldsymbol{r}) + Q^{aniso}_{s,g}(\boldsymbol{r}, \boldsymbol{\Omega}) \tag{2}$$

where $Q_{f,g}(\boldsymbol{r})$ is the fission source term and the scattering source terms include both isotropic $Q^{iso}_{s,g}(\boldsymbol{r})$ and anisotropic $Q^{aniso}_{s,g}(\boldsymbol{r}, \boldsymbol{\Omega})$scattering. The boundary condition is given by

$$\varphi_g(r, \Omega) = f(r, \Omega) \quad r = \partial R, \Omega \cdot n < 0. \tag{3}$$

which means that the incoming angular flux is distributed as the function f on the external boundary.

The MOC equation provides a solution of the Boltzmann Transport equation along a line in a particular direction and it reduces to the total differential Eq. (4) which is simplified by removing the energy group subscript g.

$$\frac{d\varphi(\boldsymbol{r}_0 + s\boldsymbol{\Omega}_m, \boldsymbol{\Omega}_m)}{ds} + \Sigma_t(\boldsymbol{r}_0 + s\boldsymbol{\Omega}_m)\varphi(\boldsymbol{r}_0 + s\boldsymbol{\Omega}_m, \boldsymbol{\Omega}_m) = Q(\boldsymbol{r}_0 + s\boldsymbol{\Omega}_m, \boldsymbol{\Omega}_m) \tag{4}$$

where $\boldsymbol{r}_0$ is the starting point of a characteristic line and s is the distance from the initial point to the current point along a specified direction $\boldsymbol{\Omega}_m$.

When solving the equation, we assume that the source and properties are constant in a small region D_i.

$$Q(\boldsymbol{r}, \boldsymbol{\Omega}_m) = Q_i(\boldsymbol{\Omega}_m), \quad \Sigma_t(\boldsymbol{r}_0 + s\boldsymbol{\Omega}_m) = \Sigma_{t,i}, \quad \boldsymbol{r} \in D_i.$$

In this small region if we know the incoming angular flux along the line k which starts at the boundary $\boldsymbol{r}_0 \in \partial D_i$ and which can be written as $\varphi^{in}_{i,k}(\boldsymbol{\Omega}_m)$, then the MOC equation has the analytic solution along this line in the region D_i.

$$\varphi_{i,k}(\boldsymbol{r}_0 + s\boldsymbol{\Omega}_m, \boldsymbol{\Omega}_m) = \varphi^{in}_{i,k}(\boldsymbol{\Omega}_m)\exp\left(-\Sigma_{t,i}s\right) + \frac{Q_{i,k}(\boldsymbol{\Omega}_m)}{\Sigma_{t,i}}\left[1 - \exp\left(-\Sigma_{t,i}s\right)\right]. \tag{5}$$

The outgoing angular flux from D_i along the line can then be calculated as:

$$\varphi^{out}_{i,k}(\boldsymbol{\Omega}_m) = \varphi^{in}_{i,k}(\boldsymbol{\Omega}_m)\exp\left(-\Sigma_{t,i}s_{i,k}\right) + \frac{Q_{i,k}(\boldsymbol{\Omega}_m)}{\Sigma_{t,i}}\left[1 - \exp\left(-\Sigma_{t,i}s_{i,k}\right)\right], \tag{6}$$

where $s_{i,k}$ is the length between the outgoing point and the incoming point of the line k in D_i. The average segment angular flux can then be given as:

$$\overline{\varphi}_{i,k}(\boldsymbol{\Omega}_m) \cdot s_{i,k} = \frac{Q_{i,k}(\boldsymbol{\Omega}_m)}{\Sigma_{t,i}} s_{i,k} + \frac{\varphi^{in}_{i,k}(\boldsymbol{\Omega}_m) - \varphi^{out}_{i,k}(\boldsymbol{\Omega}_m)}{\Sigma_{t,i}}. \tag{7}$$

2.2. Method of characteristics direction probabilities

The three-dimensional characteristics direction probabilities (CDP) include the directional transmission and collision probabilities which are stored for all the unique geometries of the problem. The transmission and collision probabilities are derived from the MOC Eq. (5). For a given geometry sub-domain (see Fig. 1), the outgoing angular flux can be written in terms of the probabilities as:

$$\varphi^{out}_{i,k}(\boldsymbol{\Omega}_m) = T_{k,in->out}(\boldsymbol{\Omega}_m)\varphi^{in}_{j=1,k}(\boldsymbol{\Omega}_m) + \sum_{j=1}^{i} T_{k,\,j->out}(\boldsymbol{\Omega}_m) Q_{j,k}(\boldsymbol{\Omega}_m), \tag{8}$$

where k is the characteristic line index and i is the flat source region index along the characteristic line shown in Fig. 1, and where $j = 1$ is

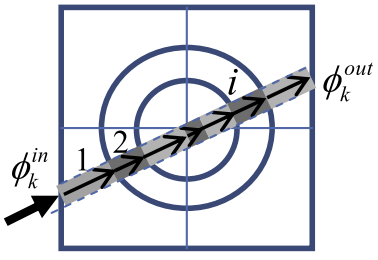

Fig. 1. The modular geometry sub-domain.

the first region traversed by the characteristic line k , and where $\varphi_{i,k}^{out}(\Omega_m)$ and $\varphi_{j=1,k}^{in}(\Omega_m)$ represent the outgoing angular flux and incoming angular flux along the characteristic line k of the sub-domain, respectively. In Eq. (8), the transmission probabilities can be calculated by substituting $\varphi_{i,k}^{in}(\Omega_m) = \varphi_{i-1,k}^{out}(\Omega_m)$ into Eq. (6) recursively until $i-1=1$.

$$T_{k,in->out}(\boldsymbol{\Omega}_m) = \exp\left(-\sum_{j=1}^{i}(\Sigma_{t,j}s_{j,k})\right)$$
$$T_{k,j->out}(\boldsymbol{\Omega}_m) = \frac{1}{\Sigma_{t,j}}\left[1-\exp\left(-\Sigma_{t,j}s_{j,k}\right)\right]\exp\left(-\sum_{l=j+1}^{i}\Sigma_{t,l}s_{l,k}\right) \tag{9}$$

where $j+1$ is the next fine mesh region index of jth region in the down-streaming direction.In addition to the outgoing angular flux, the segment average angular flux of the fine mesh region can be obtained by substituting Eq. (8) and $\varphi_{i,k}^{in}(\boldsymbol{\Omega}_m) = \varphi_{i-1,k}^{out}(\boldsymbol{\Omega}_m)$ into Eq. (7) and then expressing it in terms of the incoming angular flux and fine mesh region source of the sub-domain.

$$\overline{\varphi}_{i,k}(\boldsymbol{\Omega}_m)s_{i,k} = P_{k,in->i}\varphi_{1,k}^{in}(\boldsymbol{\Omega}_m) + \sum_{j=1}^{i}P_{k,j->i}Q_{j,k}(\boldsymbol{\Omega}_m), \tag{10}$$

where

$$P_{k,in->i}(\boldsymbol{\Omega}_m) = \frac{\exp\left(-\sum_{j=1}^{i-1}(\Sigma_{t,j}s_{j,k})\right)\left[1-\exp\left(-\Sigma_{t,i}s_{i,k}\right)\right]}{\Sigma_{t,i}}$$
$$P_{k,j->i}(\boldsymbol{\Omega}_m) = \begin{cases} \frac{s_{i,k}\Sigma_{t,i}-\left[1-\exp\left(-\Sigma_{t,i}s_{i,k}\right)\right]}{\Sigma_{t,i}\Sigma_{t,i}}; & j=i \\ \frac{\left[1-\exp\left(-\Sigma_{t,j}s_{j,k}\right)\right]\exp\left(-\sum_{l=j+1}^{i-1}\Sigma_{t,l}s_{l,k}\right)\left[1-\exp\left(-\Sigma_{t,i}s_{i,k}\right)\right]}{\Sigma_{t,j}\Sigma_{t,i}}; & j\neq i \end{cases} \tag{11}$$

When the average is determined, the boundary is divided into several sub-boundaries as shown in Fig. 2. Then the outgoing angular flux of the sub-boundary will be:

$$\varphi_{bo}^{out}(\boldsymbol{\Omega}_m) = \sum_{bi\in N(bo)}T_{bi->bo}(\boldsymbol{\Omega}_m)\varphi_{bi}^{in}(\boldsymbol{\Omega}_m) + \sum_{j\in J(bo)}T_{j->out}(\boldsymbol{\Omega}_m)Q_{j,k}(\boldsymbol{\Omega}_m), \tag{12}$$

where

$$T_{bi->bo}(\boldsymbol{\Omega}_m) = \sum_{k\in(bo\cap bi)}\frac{A_kT_{k,in->out}(\boldsymbol{\Omega}_m)}{A_{bo}},$$
$$T_{j->bo}(\boldsymbol{\Omega}_m) = \sum_{k\in(bo\cap j)}\frac{A_kT_{k,j->out}(\boldsymbol{\Omega}_m)}{A_{bo}}, \tag{13}$$

where $N(bo)$ is the total number of incoming sub-boundaries that will be traversed by the characteristic going through sub-boundary bo , $J(bo)$ is the total number of sub-domains whose source will contribute to the sub-boundary bo , A_k is the cross-sectional area of the characteristic track orthogonal to the characteristic track direction, A_{bo} is the projection area of the sub-boundary, and $k\in(bo\cap bi)$ means the characteristic lines traverse both the bi and bo sub-boundaries.

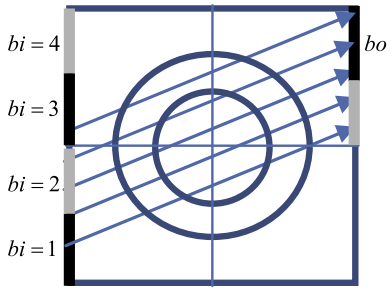

Fig. 2. The sub-boundaries of a sub-domain.

Eq. (10) can then be used to calculate the segment average angular flux. The region average angular flux can be derived by summing all segment average angular fluxes in the region D_i:

$$\overline{\varphi}_i(\boldsymbol{\Omega}_m) = \frac{\sum_{k\in i}\overline{\varphi}_{i,k}(\boldsymbol{\Omega}_m)s_{i,k}A_{i,k}}{V_i}. \tag{14}$$

By substituting Eq. (10) into Eq. (14) and expressing it in terms of the incoming angular fluxes and fine mesh region sources, the region average angular flux can then be determined:

$$\overline{\varphi}_i(\boldsymbol{\Omega}_m) = \sum_{bi\in N(i)}\left(P_{bi->i}(\boldsymbol{\Omega}_m)\varphi_{bi}(\boldsymbol{\Omega}_m)\right) + \sum_{j\in up(i)}P_{j->i}(\boldsymbol{\Omega}_m)Q_{j,k}(\boldsymbol{\Omega}_m), \tag{15}$$

where

$$P_{bi->i}(\boldsymbol{\Omega}_m) = \frac{\sum_{k\in(bi\cap i)}P_{k,in->i}(\boldsymbol{\Omega}_m)A_{i,k}}{V_i} = \sum_{k\in(bi\cap i)}\frac{A_{i,k}}{\Sigma_{t,i}V_i}\exp\left(-\sum_{j=1}^{i-1}(\Sigma_{t,j}s_{j,k})\right)\left[1-\exp\left(-\Sigma_{t,i}s_{i,k}\right)\right], \tag{16}$$

and

$$P_{j->i}(\boldsymbol{\Omega}_m) = \begin{cases} \sum_{k\in(i)}\frac{\left(s_{i,k}\Sigma_{t,i}-\left[1-\exp\left(-\Sigma_{t,i}s_{i,k}\right)\right]\right)A_{i,k}}{V\Sigma_{t,i}\Sigma_{t,i}}; & j=i \\ \sum_{k\in(i\cap j)}\frac{\left[1-\exp(-\Sigma_{t,j}s_{j,k})\right]\exp\left(-\sum_{l=j+1}^{i-1}\Sigma_{t,l}s_{l,k}\right)\left[1-\exp\left(-\Sigma_{t,i}s_{i,k}\right)\right]A_{i,k}}{V_i\Sigma_{t,j}\Sigma_{t,i}}; & j\neq i \end{cases} \tag{17}$$

In Eq. (15), $j\in up(i)$ refers to the regions in the up-streaming direction of region i, and in Eq. (17) $k\in(i\cap j)$ refers to the characteristic lines which traverse through both region i and j. Therefore the region average angular flux couples all the incoming angular fluxes which traverse through this region and the fine mesh regions in the up-stream direction.

The following reciprocity relations follow directly from Eqs. (17), (16) and (9):

$$P_{j->i}(\boldsymbol{\Omega}_m)V_i = P_{i->j}(\Omega_m)V_j \tag{18}$$

$$P_{k,bi->i}(\boldsymbol{\Omega}_m)V_i = T_{k,i->bi}(\boldsymbol{\Omega}_m)A_{bi} \tag{19}$$

and

$$T_{bi->bo}(\boldsymbol{\Omega}_m)A_{bo} = T_{bo->bi}(\boldsymbol{\Omega}_m)A_{bi} \tag{20}$$

A compact linear expression for calculating the outgoing angular flux and region average angular fluxes in the modular geometry sub-domain can be formed using Eqs. (12) and (15):

$$\begin{bmatrix}\vec{\varphi}^{out}\\ \vec{\phi}\end{bmatrix} = A\begin{pmatrix}\vec{\varphi}^{in}\\ \vec{Q}\end{pmatrix} \tag{21}$$

and,

$$\vec{\varphi}^{out} = \begin{bmatrix}\varphi_{bo=1}^{out}(\boldsymbol{\Omega}_m)\\ \varphi_{bo=2}^{out}(\boldsymbol{\Omega}_m)\\ \vdots\\ \varphi_{bo=K}^{out}(\boldsymbol{\Omega}_m)\end{bmatrix}, \vec{\phi} = \begin{bmatrix}\phi_{i=1}(\boldsymbol{\Omega}_m)\\ \phi_{i=2}(\boldsymbol{\Omega}_m)\\ \vdots\\ \phi_{i=I}(\boldsymbol{\Omega}_m)\end{bmatrix},$$
$$\vec{\varphi}^{in} = \begin{bmatrix}\varphi_{bi=1}^{in}(\boldsymbol{\Omega}_m)\\ \varphi_{bi=2}^{in}(\boldsymbol{\Omega}_m)\\ \vdots\\ \varphi_{bi=K}^{in}(\boldsymbol{\Omega}_m)\end{bmatrix}, \vec{Q} = \begin{bmatrix}Q_{i=1}(\boldsymbol{\Omega}_m)\\ Q_{i=2}(\boldsymbol{\Omega}_m)\\ \vdots\\ Q_{i=I}(\boldsymbol{\Omega}_m)\end{bmatrix}. \tag{22}$$

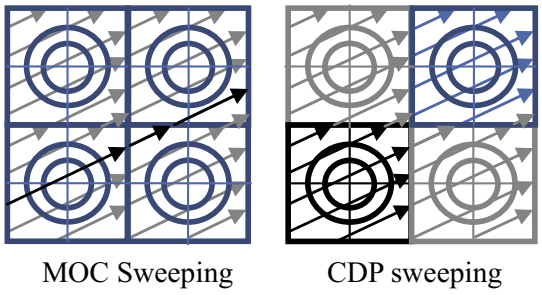

Fig. 3. The sweeping order for MOC and CDP.

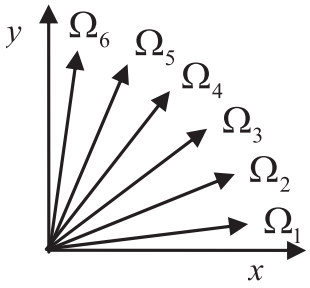

Fig. 5. Six azimuthal angles.

where $\vec{\varphi}^{out}$ and $\vec{\varphi}^{in}$ are the outgoing and incoming angular fluxes of the all sub-boundaries of the geometry sub-domain, which have the same number of the sub-boundaries, and $\bar{\phi}$ and $\bar{Q}$ are the region average angular fluxes and region angular source of the fine regions. The matrix A contains all the transmission and collision probabilities described in Eqs. (17), (16) and (13). If the incoming angular flux and region sources are known, then the outgoing angular fluxes and region average angular flux can be directly calculated with this linear system.

The sweeping iteration for MOC and CDP is compared for a 2×2 array of pins as shown in Fig. 3. In the left side of Fig. 3, a typical sweeping strategy is shown for the conventional MOC in which the ray tracing is performed ray by ray (note the hard black lines), while on the right side of the figure the CDP sweep is performed sub-domain by sub-domain. For a given initial value of the incoming angular flux of the system, the outgoing angular fluxes and region average angular fluxes of the left bottom sub-domain can be obtained by Eq. (21). The same calculations are then performed on the right bottom sub-domain and the left top sub-domain until all modular sub-domains are swept. For the direction shown in Fig. 3, the sweeping begins from the left bottom corner, but for the opposite direction the first sub-domain to be computed is from the right top corner. So the sweeping order is different for the directions in different octants.

3. The angle dependent boundary averaging method

3.1. Analysis of the boundary angular fluxes

Averaging of the boundary angular fluxes can reduce the computational effort, but could potentially compromise the accuracy of the solution. A detailed analysis was performed on the impact of averaging by using a sequence of typical cell problems with cross sections from the C5G7 Benchmark. The first case analyzed was a single pin cell with reflective boundaries and six azimuthal angles as shown in Figs. 4 and 5.

The outgoing angular fluxes on the right boundary for the first energy group are tallied for different angles as shown in Fig. 6. In this figure the magnitude of the angular flux (y-axis) is shown at various points from the bottom to the top of the pin boundary (x-axis). These results indicate that: the variation of the angular flux of the 6th angle is relatively smooth while the variation for smaller angles is more pronounced when moving along the boundary from the bottom to the top of the pin.

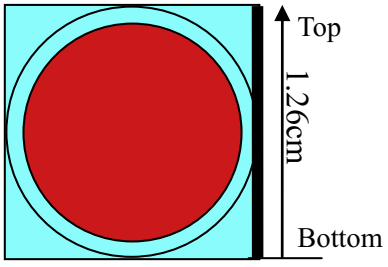

Fig. 4. The cell configuration.

In order to understand the reasons for the variation, a detailed analysis was performed of the dependence of the outgoing angular flux on the incoming angular flux, the internal sources, and the optical thickness as shown in Eq. (22):

$$\varphi_{i,k}^{out}(\Omega_{\boldsymbol{m}}) = \varphi_{\boldsymbol{i,k}}^{in}(\Omega_{\boldsymbol{m}})exp(-\Sigma_{\boldsymbol{t,i}}\boldsymbol{s_{i,k}}) + \frac{\boldsymbol{Q_{i,k}}(\Omega_{\boldsymbol{m}})}{\Sigma_{\boldsymbol{t,i}}}[\boldsymbol{1} - exp(-\Sigma_{\boldsymbol{t,i}}\boldsymbol{s_{i,k}})] \tag{23}$$

In order to assess the impact of the source distribution, three different pin cell cases were run with different mesh as shown in Fig. 7. All three cases gave the same results as shown in Fig. 6, which suggest that the variation of the angular flux at the boundary is not dominated by the source and the mesh discretization.

In order to investigate the impact of the incoming angular flux on the variation of the angular flux on the boundary, a larger case was run with an 8×8 array of pin cells as shown in Fig. 8. This problem was performed with the vacuum boundary condition on the left face and reflective boundary conditions on other faces. In order to understand the results, it is instructive to first look at the impact of only the first angle on the outgoing angular flux on the right boundary as shown in Fig. 8. As indicated, only the regions between the two black lines contribute to the outgoing angular flux on the right face of the right-top pin. In order to more easily understand the variation in the outgoing flux at the boundary it is instructive to express the flux as the sum of the contributions of the fluxes from each of the eight columns of pins (Note that the pins are numbered from right to left on the x-axis in Fig. 8). The outgoing angular flux can then be calculated by:

$$\begin{aligned} \varphi_k^{out} &= \sum_n \widehat{\varphi}_{n,k}^{out} w_{n,k} \\ \widehat{\varphi}_{n,k}^{out} &= \int_0^{S_n} Q_n(s)exp(-\Sigma_{t,s}(s_n - s))\mathrm{ds} \\ w_{n,k} &= exp\left(-\int \Sigma_{t,s,k}ds\right) \end{aligned} \tag{24}$$

where $\widehat{\varphi}_{n,k}^{out}$ is the outgoing angular flux of the column n along the kth line without incoming angular flux; $w_{n,k}$ is contribution weight of the nth column along the kth line to the final outgoing angular flux; $\int \Sigma_{t,s,k}ds$ is the optical thickness from the nth column to the final outgoing boundary along the kth line.

The outgoing angular flux, $\widehat{\varphi}_{n,k}^{out}$, can be obtained by integrating the characteristic equation along the line analytically or by simply performing the calculation with the vacuum boundary condition on the left. Fig. 9 shows the contributions of the first three columns to the group 1 angular flux at the right boundary of the top pin in column 1.

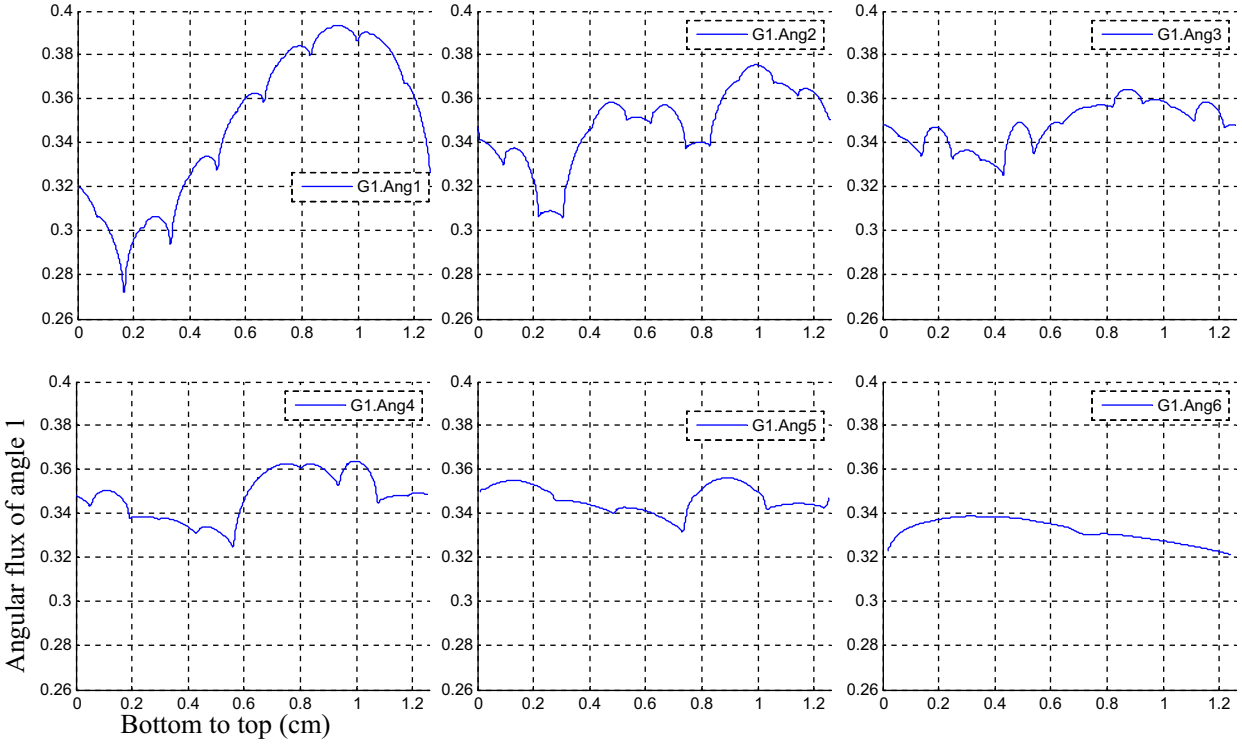

Fig. 6. The outgoing angular flux of the first group for different angles.

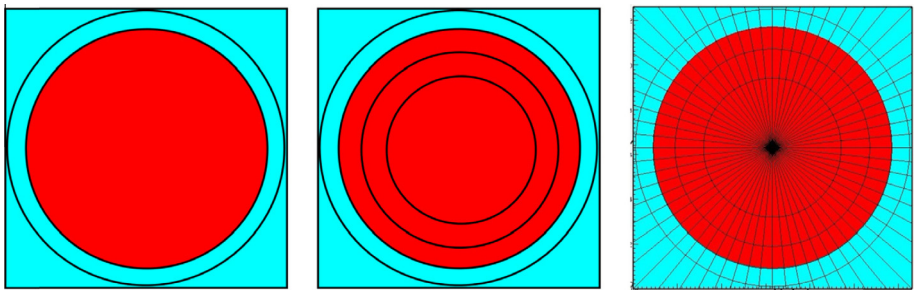

Fig. 7. Different Pin Cell Mesh Discretizatoin.

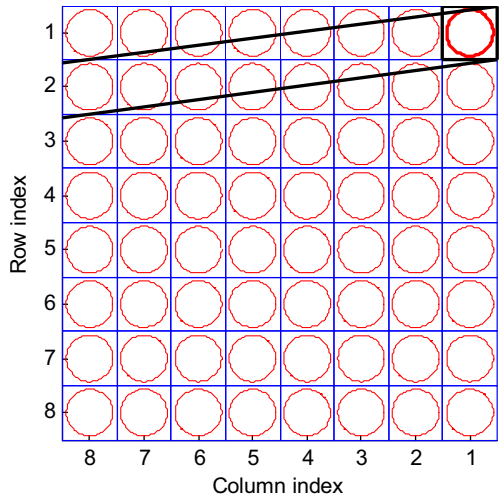

Fig. 8. 8 by 8 pin configuration.

It is apparent that:

(1) The variation of the angular flux of every column is relatively simple since it rises when the characteristic line traverses the fuel, and decreases when the characteristic lines leaves the fuel;
(2) The shape of variation is the same but shifts some distance to right side for columns 2 and 3 which can be explained by examining the outgoing boundary position of every column as shown in Fig. 8.

The contribution weight in Eq. (23) is dependent on the total cross section and the segment length in the fuel and moderator. However, because the difference of the group 1 total cross sections between the fuel and moderator is small, the calculation of the contribution weights can be simplified by using the average total cross sections. The weights would then be constant for every column and can be calculated using:

$$w_n = exp\left(-\int \Sigma_{t,s} ds\right) = exp\left(-(n-1)\Sigma_{t,average} s_{column}\right) \quad (25)$$

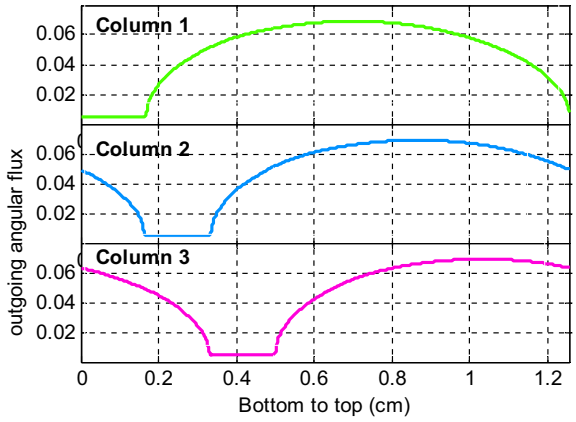

Fig. 9. The outgoing angular flux of the first 3 columns.

where, n is the column index; $\Sigma_{t,average}$ is the average total cross section of the fuel and moderator; s_{column} is the length traversed by the characteristic line in one column. The contribution weights of every column for each angle can be determined using Table 1.

According to Table 1, only the first 8 columns are considered for the first angle since the weight of the 9th column would be less than 10%. Therefore, it can be neglected for purposes here of understanding the variation of the right boundary flux on the pin in column 1. In Fig. 10, the bottom-right part inset shows the contribution of every column considering its contribution weight as well as the final outgoing angular flux in the top portion of the inset. As indicated, the lowest point in magnitude highlighted in the figure occurs when the line enters the fuel of the first column and exits the second column. This inflection point occurs whenever the line is coming out of the fuel region in one column or going into the fuel region in another column.

The variations of the other angles are slightly more complicated, but they can be simulated using the same methods. As an example the results for the third angle are shown in Fig. 11.

The observations above will contribute to the understanding of the accuracy achievable for each of the averaging cases used in the following sections. This analysis will also provide a physical basis for selecting an averaging that depends on the angle.

3.2. The angle dependent boundary averaging method

Similar to the MOC modular ray tracing technique, the ray tracing information for the method of Boundary Averaged Characteristics Direction Probabilities is stored for all unique sub-domains as shown in Fig. 12. The easiest way to perform the averaging is to define a fixed number of sub-boundaries on each face of the cell. However, this method does not consider the fact that the shape of the outgoing flux is different for different angles and groups. So an angle dependent boundary averaging method is introduced. For purposes of describing the boundary averaging process, it is useful to introduce the coarse ray spacing of the radial

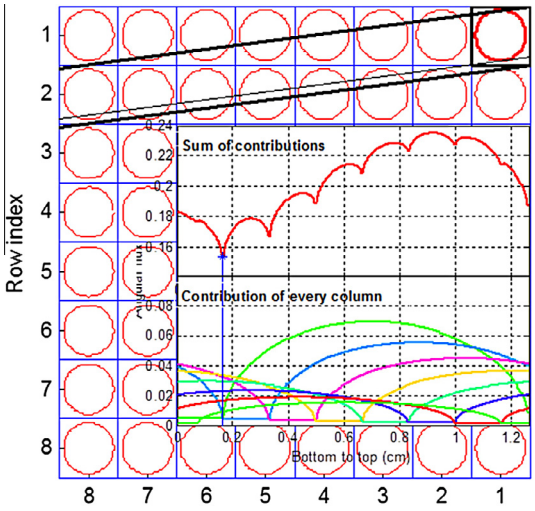

Fig. 10. The final outgoing angular flux shape of the first angle.

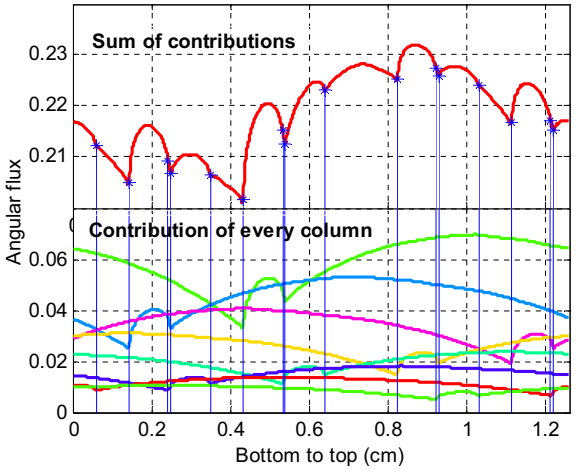

Fig. 11. The outgoing angular flux of the third angle.

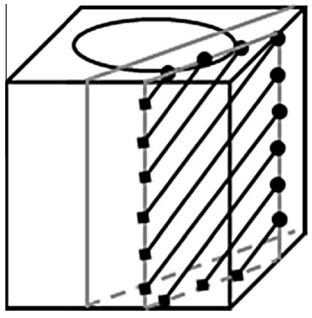

Fig. 12. The characteristic rays of a sub-domain.

Table 1
The contribution weights.

Column	1	2	3	4	5	6	7	8
Angle 1	**1.0E+0**	**7.4E−1**	**5.5E−1**	**4.1E−1**	**3.0E−1**	**2.2E−1**	**1.6E−1**	**1.2E−1**
Angle 2	**1.0E+0**	**7.2E−1**	**5.2E−1**	**3.8E−1**	**2.7E−1**	**2.0E−1**	**1.4E−1**	**1.0E−1**
Angle 3	**1.0E+0**	**6.9E−1**	**4.7E−1**	**3.2E−1**	**2.2E−1**	**1.5E−1**	**1.0E−1**	7.2E−2
Angle 4	**1.0E+0**	**6.1E−1**	**3.8E−1**	**2.3E−1**	**1.4E−1**	8.7E−2	5.3E−2	3.3E−2
Angle 5	**1.0E+0**	**4.6E−1**	**2.1E−1**	**9.7E−2**	4.5E−2	2.0E−2	9.5E−3	4.4E−3
Angle 6	**1.0E+0**	**1.0E−1**	1.0E−2	1.1E−3	1.1E−4	1.1E−5	1.2E−6	1.2E−7

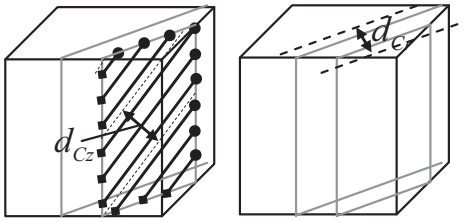

Fig. 13. The coarse ray spacing.

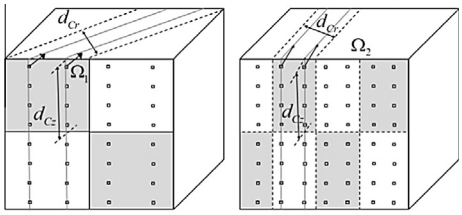

Fig. 15. Boundary index average of the other faces.

direction (see Fig. 13.d_{Cr}) and the coarse ray spacing of z-axial direction (see Fig. 13.d_{Cz}).

The average is performed for all faces, respectively, and it is different for the TOP/BOTTOM faces than for the other faces. As shown in Fig. 14 for the TOP/BOTTOM faces, the boundary indices coming from the same flat source region between coarse rays are averaged together. So only the coarse ray spacing of the radial direction is useful when the average is determined for the TOP/BOTTOM faces. This averaging method has the benefit that at the same time it can determine all the outgoing fluxes which are outgoing from the same flat source region but in different angles and space (see the right two figures in Fig. 15).

The average of the other faces is performed on every sub-boundary which is determined by the coarse rays shown in Fig. 15. This averaging strategy defines different number of sub-boundaries on the face for different angles, which is consistent with the shape of the outgoing flux on the face. The angles for which the shape change is most dramatic will have more sub-boundaries as shown in Fig. 15.

4. Numerical results

The accuracy of the boundary-averaged CDP method proposed here were evaluated using two test problems. The first is a 2D pin case, and the second is a standard reactor benchmark published by Takeda and Ikeda (1991).

4.1. The 2D pin case

This 2D problem is designed to analyze the impact of averaging on the outgoing angular flux, region flux and eigenvalue. The configuration of the pin is the same with Fig. 4 and C5G7 cross-sections are used as well. The angular quadrature of six azimuthal angles and one polar angle are applied to show the impact of averaging for different angles. The ray spacing is 0.03 cm and three different coarse ray spacing are chosen: (1) 0.06 cm, (2) 0.1 cm (3) 0.2 cm, and case 3 is relatively aggressive to show the trend while the ray spacing of coarse rays grows. All the results are compared to the case without average which gives an identical result to the MOC solution.

The right boundary angular fluxes are tallied for several angles and groups. In Fig. 16, the first group's outgoing angular fluxes of angle 1 are given for both reference and case 3, and the relative difference is shown at the same time. More comparisons for other cases are demonstrated in Figs. 17–23.

The outgoing angular fluxes of group 1 for different angles are given in Figs. 17–19. The outgoing angular fluxes of angle 1 for different groups are shown in Figs. 17, 20 and 21. It can be concluded that the difference of outgoing angular flux increases as the coarse ray spacing grows. For the first two cases, the difference of boundary angular fluxes for different angles and different groups are relatively small, indicating that appropriate coarse ray spacing will gives satisfying angular flux shape. Even for the more aggressive averaging of case three, only angular fluxes of several points exceed 2%, because 7 flat angular fluxes is not enough to describe the details of the angular flux shown in case3.

The eigenvalues for all cases are shown in Table 2. As indicated the eigenvalues for the first two cases agree well with the reference because the boundary averaging in these cases provides a better approximation of the outgoing angular fluxes, and the eigenvalues of case 3 just has 30 pcm difference. The differences of the scalar fluxes for all flat source regions are shown in Fig. 22, from which it can be seen that the differences of scalar fluxes of all flat source regions for all groups are less than 1%. 1% differences occur at the regions closed to the boundary because of the about 2% difference of the several boundary angular fluxes.

4.2. KUCA Takeda core benchmark

The Kyoto University Critical Assembly (KUCA) benchmark was published by Takeda and Ikeda in 1991 (Takeda and Ikeda, 1991). This problem models a small Light Water reactor core of dimensions 50 cm × 50 cm × 50 cm, with three material regions including fuel, control rod, and reflector. Fig. 23 shows the core configuration and the 2 group cross section are provided in Appendix A. The control rod worth was evaluated for this problem by inserting and removing the control rod.

The two cases were performed with identical discretizations in which the sub-domain size was 1 cm × 1 cm × 1 cm with 32 fine-regions in each sub-domain. The ray spacing was 0.03 cm and an S4 angular quadrature sets was used in all cases. The results

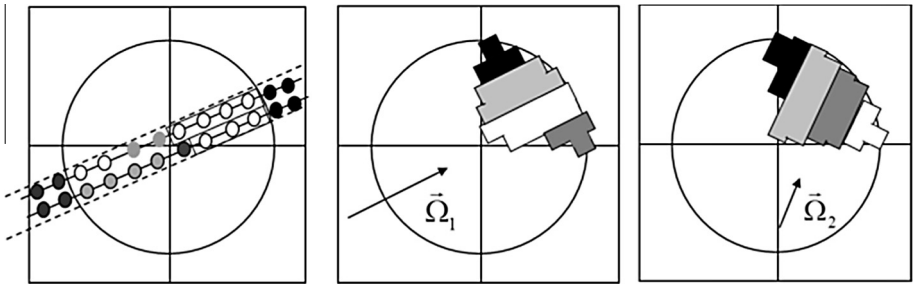

Fig. 14. Boundary index average of the TOP/BOTTOM face.

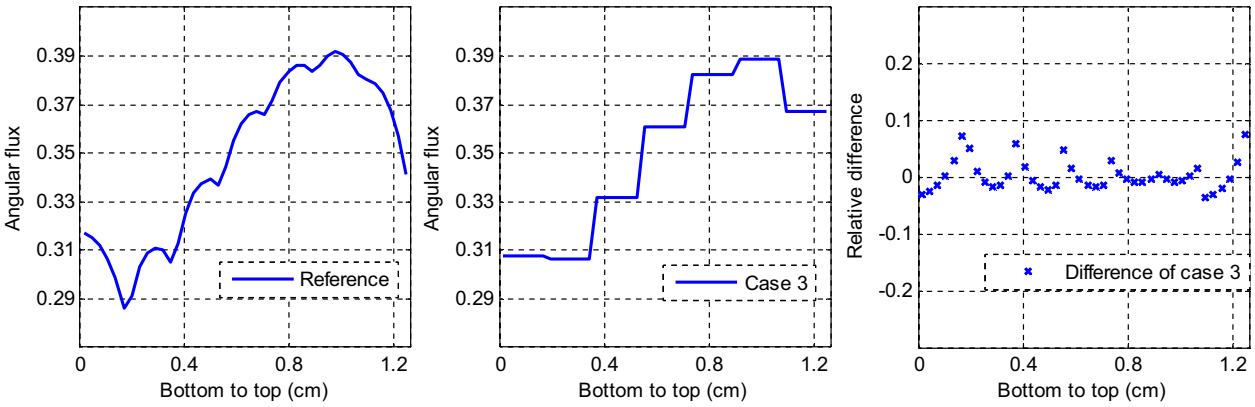

Fig. 16. The first group's outgoing angular flux of angle 1 and the difference between Case 3 and reference.

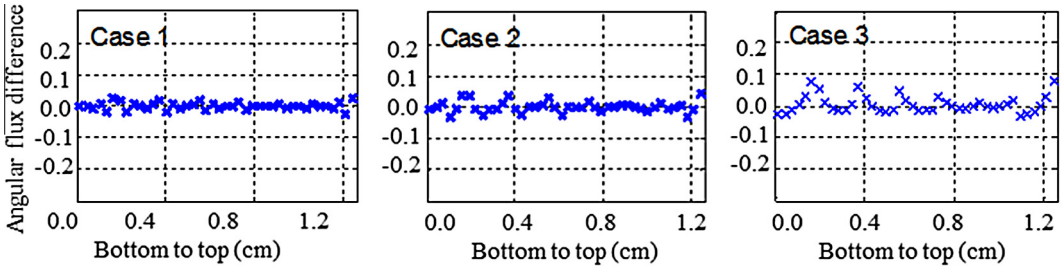

Fig. 17. The relative difference of outgoing angular flux of group 1 of the first angle.

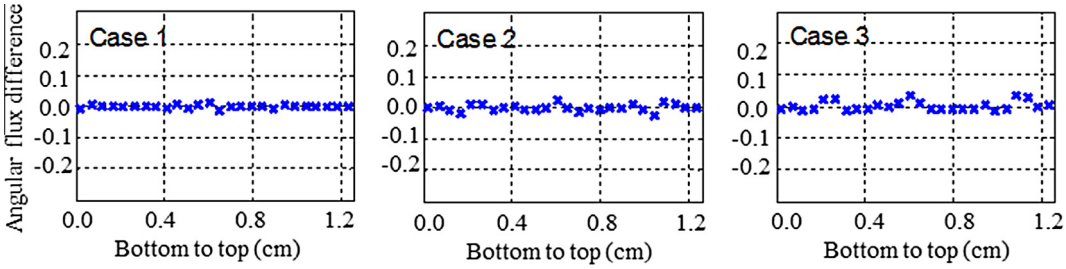

Fig. 18. The relative difference of outgoing angular flux of group 1 of the forth angle.

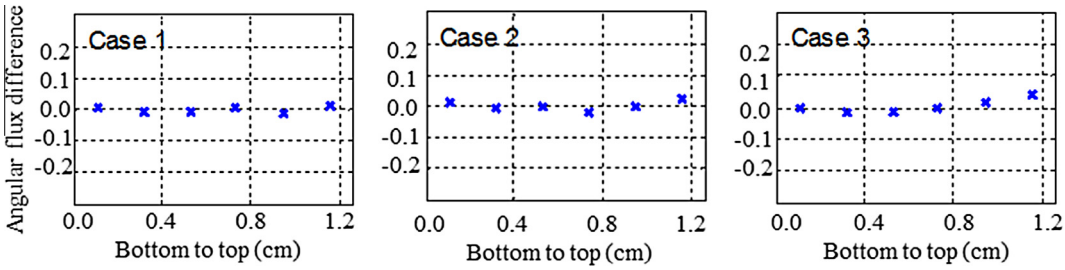

Fig. 19. The relative difference of outgoing angular flux of group 1 of the sixth angle.

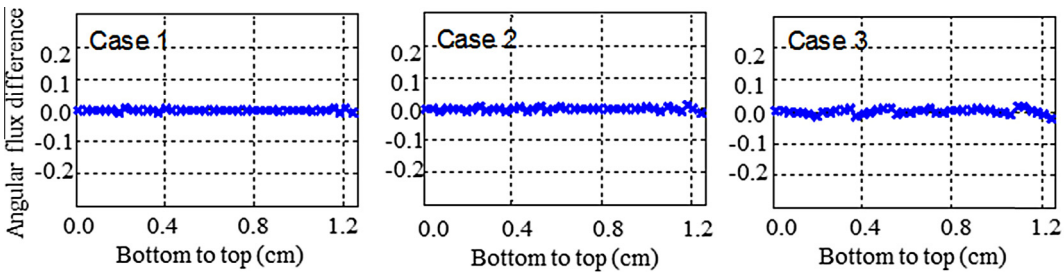

Fig. 20. The relative difference of outgoing angular flux of group 5 of the first angle.

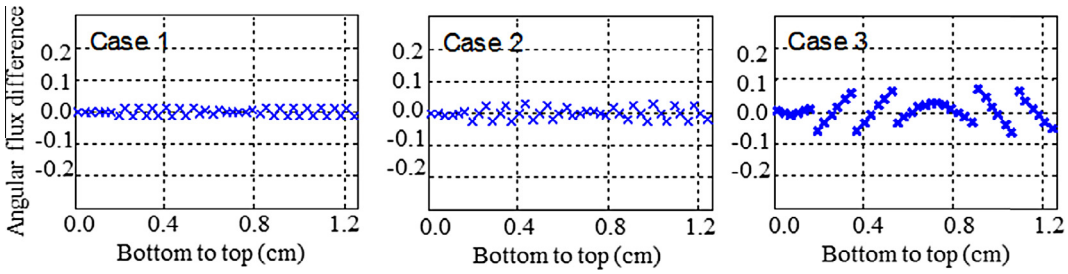

Fig. 21. The relative difference of outgoing angular flux of group 7 of the first angle.

Table 2
The keff of the pin problem.

No_average	Case 1	Case 2	Case 3
1.32528	1.32531	1.32536	1.32558

Table 3
Comparison of k-eff for KUCA Benchmark.

Method	UnRodded	Rodded	CR-worth
Ref Monte Carlo	0.9780	0.9624	1.66E−02
	±0.0006	±0.0006	±0.09E−2
MOC	0.9776	0.9627	1.59E−02
CDP_case1	0.9776	0.9627	1.59E−02
CDP_case2	0.9773	0.9624	1.59E−02
CDP_case3	0.9769	0.9619	1.59E−02

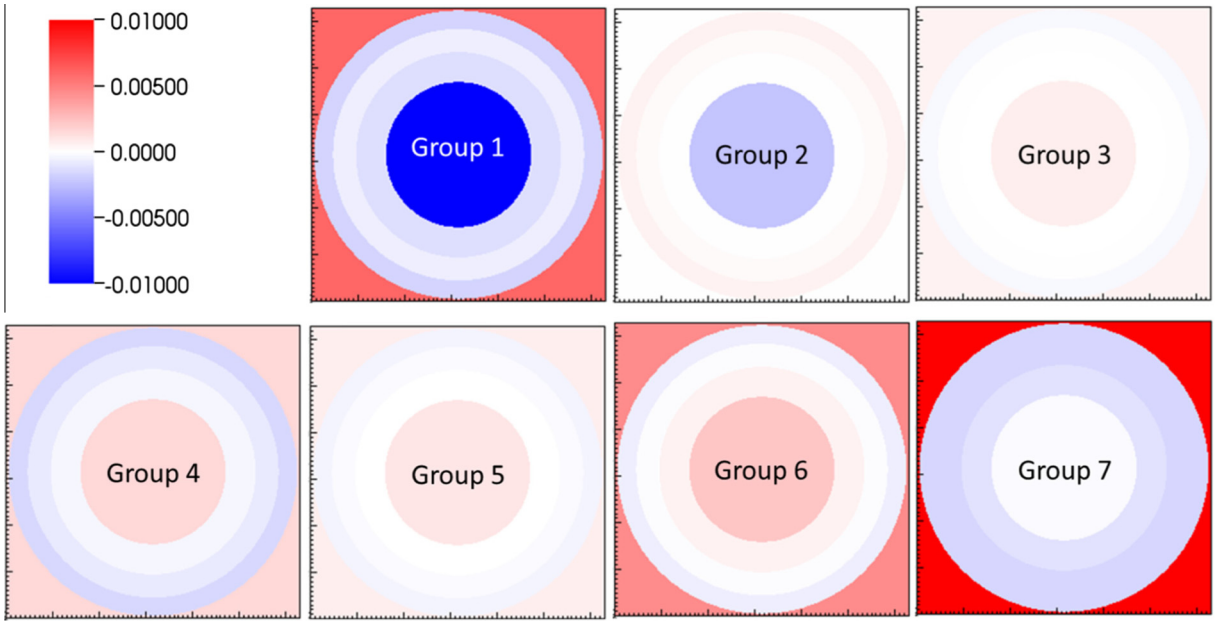

Fig. 22. The relative difference of scalar flux for case 2.

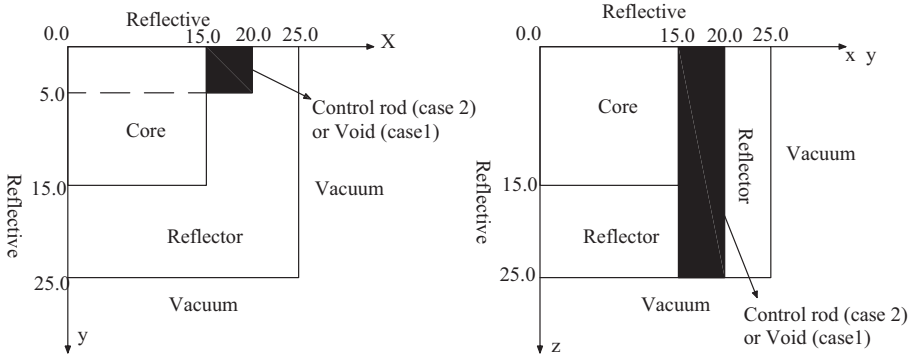

Fig. 23. KUCA core benchmark core configuration.

Table 4
Computing time comparison.

Group	UnRodded				Rodded			
	MOC	CDP_case1	CDP_case2	CDP_case3	MOC	CDP_case1	CDP_case2	CDP_case3
Total time/s	3357.8	1041.04	273.69	119.28	3494.5	916.01	272.08	116.7
Speedups	–	3.2	12.3	28.2	–	3.8	12.8	29.9

Table 5
Comparison of Region-averaged fluxes.

Method	Group	UnRodded			Rodded		
		Core	Reflector	Void	Core	Reflector	CR
Ref Monte-Carlo	1	4.7509E−03	5.9251E−04	1.4500E−03	4.9125E−03	5.9109E−04	1.2247E−03
		0.10%	0.21%	0.47%	0.10%	0.21%	0.48%
	2	8.6998E−04	9.1404E−04	9.7406E−04	8.6921E−04	8.7897E−04	2.4604E−04
		0.12%	0.23%	0.63%	0.13%	0.23%	0.72%
MOC	1	−0.36%	0.86%	3.01%	−0.87%	0.30%	1.70%
	2	0.32%	−1.43%	−0.98%	−0.08%	−1.56%	0.10%
CDP_case1	1	−0.36%	0.86%	3.01%	−0.87%	0.30%	1.70%
	2	0.32%	−1.43%	−0.98%	−0.08%	−1.56%	0.10%
CDP_case2	1	−0.37%	0.89%	3.00%	−0.88%	0.34%	1.72%
	2	0.32%	−1.58%	−1.09%	−0.08%	−1.70%	0.21%
CDP_case3	1	−0.39%	0.94%	2.97%	−0.91%	0.40%	1.70%
	2	0.32%	−1.84%	−1.26%	−0.08%	−1.97%	0.16%

include the reference Monte Carlo and MOC as well as the CDP results with three different averaging cases:

(1) CDP_Case1: CDP calculation without average,
(2) CDP_Case2: CDP averaged with the coarse ray spacing of 0.03 cm in the radial plane and 0.15 cm in the axial direction,
(3) CDP_Case3: CDP averaged with the coarse ray spacing of 0.1 cm in the radial plane and 0.3 cm in the axial direction.

The reference results of the Monte-Carlo method were provided in reference (Takeda and Ikeda, 1991) and the k-eff and control rod worth $(k - k')/(kk')$ are compared to these results in Table 3. As expected, the CDP without average is consistent to the MOC, and the average introduces some discrepancy in k-eff.

Because this problem has a significant axial flux distribution compared to the previous test problems, the use of a smaller number of flat source regions on the TOP/BOTTOM interfaces introduces some discrepancy in k-eff. computing efforts comparison is listed in Table 4, and the comparison of the region-averaged fluxes for the rod inserted and withdrawn is shown in Table 5.

The overall conclusion from these results is that CDP with boundary averaging can achieve more then 10 times speedup while providing satisfactory results for this problem with the above discretization.

5. Summary and conclusions

The research here investigated the method of characteristic direction probability (CDP) as a means to reduce the MOC computational time for 3D problems. The CDP combines the geometry flexibility of the MOC and the computing efficiency of the CPM that has been popularly used in lattice codes. At the same time the CDP can reduce some of the drawbacks of CPM, such as the limitations in scattering treatments, as well as the high computational overhead for calculating the probability matrices and solution of the matrix system. In the CDP method, the probabilities only couple the fine mesh regions traversed by the characteristic lines in a particular direction within a sub-domain. However the probability matrix can still be large in CDP, so the additional feature was introduced of boundary averaging which reduced the number of outgoing/incoming angular fluxes transferred between domains and computational efforts.

The impact of averaging on the accuracy of the boundary angular flux, scalar flux and eigenvalue was investigated, and the results shows that the method has the ability to adjust the coarseness of the boundary averaging to accommodate a desired accuracy and computational time. Furthermore, the numerical results provided insight about the optimal averaging strategy which would improve the performance such as using different averaging strategies for different angles. Work is continuing on the investigation of adaptive methods which will adjust the boundary averaging coarseness "on the fly" to accommodate the heterogeneity of the problem and thereby improve the performance of the method and reduce the a priori effort required by the analyst to determine the optimum coarseness of the boundary averaging regions.

In the CDP, the collision and transmission probabilities need to be calculated for each direction and group, which increases the computing effort. To minimize the computing burden, these probabilities are calculated and stored before the source iteration instead of calculating them during the sweep. It needs to be addressed that because the CDPs are dependent on energy and direction, for the fresh core, only the CDPs of the unique sub-domains are stored, but when the burnup is considered the CDPs of all sub-domains are stored, which might make the memory issue be severe. Compared to the 2D-1D decoupling MOC method, in which the axial size is relative large and be solved with diffusion or nodal methods, the axial size of 3D MOC and CDP should not be too big because of the flat source assumption.

Acknowledgements

This research was carried out under the financial support of the State Scholarship Fund of China (No. 2011628095). Thank the NERS of the University of Michigan for providing the active research environments.

Appendix A. Cross sections

Tables A.1–A.3.

Table A.1
KUCA core benchmark two-group cross sections and energy group structure for KUCA.

Region	Group	Σ_{abs}/cm^{-1}	$\nu\Sigma_{fl}/cm^{-1}$	Σ_{1-1}/cm^{-1}	Σ_{1-2}/cm^{-1}	χ
Core fuel	1	8.52709E−03	9.09319e−3	1.92423e−1	2.28253e−2	1.0
	2	1.58196E−01	2.90183e−1	0.00000E+0	8.80439e−1	
Control rod	1	1.74439E−02	0.00000E+0	6.77241e−2	6.45461e−5	–
	2	1.82224E−01	0.00000E+0	0.00000E+0	3.52358e−2	
Reflector	1	4.16392E−04	0.00000E+0	1.93446e−1	5.65042e−2	–
	2	2.02999E−02	0.00000E+0	0.00000E+0	1.62452E+0	
Empty (void)	1	4.65132E−05	0.00000E+0	1.27700e−2	2.40997e−5	–
	2	1.32890E−03	0.00000E+0	0.00000E+0	1.07387e-2	

Table A.2
Fuel-clad macroscopic cross-sections for C5G7 benchmark.

	Transport Cross-section/cm^{-1}	Absorption Cross-section/cm^{-1}	Capture Cross-section/cm^{-1}	Fission Cross-section/cm^{-1}	Nu	Chi
Group 1	1.77949E−01	8.02480E−03	8.12740E−04	7.21206E−03	2.78145E+00	5.87910E−01
Group 2	3.29805E−01	3.71740E−03	2.89810E−03	8.19301E−04	2.47443E+00	4.11760E−01
Group 3	4.80388E−01	2.67690E−02	2.03158E−02	6.45320E−03	2.43383E+00	3.39060E−04
Group 4	5.54367E−01	9.62360E−02	7.76712E−02	1.85648E−02	2.43380E+00	1.17610E−07
Group 5	3.11801E−01	3.00200E−02	1.22116E−02	1.78084E−02	2.43380E+00	0.00000E+00
Group 6	3.95168E−01	1.11260E−01	2.82252E−02	8.30348E−02	2.43380E+00	0.00000E+00
Group 7	5.64406E−01	2.82780E−01	6.67760E−02	2.16004E−01	2.43380E+00	0.00000E+00

Scattering block

	To group 1/cm^{-1}	To group 2/cm^{-1}	To group 3/cm^{-1}	To group 4/cm^{-1}	To group 5/cm^{-1}	To group 6/cm^{-1}	To group 7/cm^{-1}
Group 1	1.27537E−01	4.23780E−02	9.43740E−06	5.51630E−09	0.00000E+00	0.00000E+00	0.00000E+00
Group 2	0.00000E+00	3.24456E−01	1.63140E−03	3.14270E−09	0.00000E+00	0.00000E+00	0.00000E+00
Group 3	0.00000E+00	0.00000E+00	4.50940E−01	2.67920E−03	0.00000E+00	0.00000E+00	0.00000E+00
Group 4	0.00000E+00	0.00000E+00	0.00000E+00	4.52565E−01	5.56640E−03	0.00000E+00	0.00000E+00
Group 5	0.00000E+00	0.00000E+00	0.00000E+00	1.25250E−04	2.71401E−01	1.02550E−02	1.00210E−08
Group 6	0.00000E+00	0.00000E+00	0.00000E+00	0.00000E+00	1.29680E−03	2.65802E−01	1.68090E−02
Group 7	0.00000E+00	0.00000E+00	0.00000E+00	0.00000E+00	0.00000E+00	8.54580E−03	2.73080E−01

Table A.3
Moderator macroscopic cross-sections for C5G7 benchmark.

	Transport Cross-section/cm^{-1}	Absorption Cross-section/cm^{-1}	Capture Cross-section/cm^{-1}
Group 1	1.59206E−01	6.01050E−04	6.01050E−04
Group 2	4.12970E−01	1.57930E−05	1.57930E−05
Group 3	5.90310E−01	3.37160E−04	3.37160E−04
Group 4	5.84350E−01	1.94060E−03	1.94060E−03
Group 5	7.18000E−01	5.74160E−03	5.74160E−03
Group 6	1.25445E+00	1.50010E−02	1.50010E−02
Group 7	2.65038E+00	3.72390E−02	3.72390E−02

Scattering block

	To group 1/cm^{-1}	To group 2/cm^{-1}	To Group 3/cm^{-1}	To group 4/cm^{-1}	To group 5/cm^{-1}	To group 6/cm^{-1}	To group 7/cm^{-1}
Group 1	4.44777E−02	1.13400E−01	7.23470E−04	3.74990E−06	5.31840E−08	0.00000E+00	0.00000E+00
Group 2	0.00000E+00	2.82334E−01	1.29940E−01	6.23400E−04	4.80020E−05	7.44860E−06	1.04550E−06
Group 3	0.00000E+00	0.00000E+00	3.45256E−01	2.24570E−01	1.69990E−02	2.64430E−03	5.03440E−04
Group 4	0.00000E+00	0.00000E+00	0.00000E+00	9.10284E−02	4.15510E−01	6.37320E−02	1.21390E−02
Group 5	0.00000E+00	0.00000E+00	0.00000E+00	7.14370E−05	1.39138E−01	5.11820E−01	6.12290E−02
Group 6	0.00000E+00	0.00000E+00	0.00000E+00	0.00000E+00	2.21570E−03	6.99913E−01	5.37320E−01
Group 7	0.00000E+00	0.00000E+00	0.00000E+00	0.00000E+00	0.00000E+00	1.32440E−01	2.48070E+00

References

Cho, N.Z., 2005. Fundamentals and recent developments of reactor physics methods. Nucl. Eng. Technol. 37, 25.

Hong, S.G., Cho, N.Z., 1998. CRX: a code for rectangular and hexagonal lattices based on the method of characteristics. Annu. Nucl. Energy 25, 545–565.

Hong, S.G., Cho, N.Z., 1999. Method of characteristic direction probabilities for heterogeneous lattice calculation. Nucl. Sci. Eng. 132, 65–77.

Liu, Z., Wu, H., Cao, L., Chen, Q., Li, Y., 2011. A new three-dimensional method of characteristics for the neutron transport calculation. Annu. Nucl. Energy 38, 447–454.

Liu, Z., Kochunas, B., Collins, B., Downar, T., Wu, H., 2013. The method of modular characteristic direction probabilities in impact. In: International Conference on Mathematics and Computational Methods Applied to Nuclear Science & Engineering (M&C 2013), Sun Valley, Idaho, USA, May 5–9, 2013, on CD-ROM. American Nuclear Society, LaGrange Park, IL.

Mohanakrishnan, P., 1981. Angular current approximations in neutron transport calculations using interface current—a review. Prog. Nucl. Energy 7, 1–10.

Sanchez, R., 1977. Approximate solutions of the two dimensional integral transport equation by collision probability methods. Nucl. Sci. Eng. 64, 384–404.

Smith, K.S., Rhodes, J.D., 2000. CASMO characteristics methods for two dimensional PWR and BWR core calculations. Trans. Am. Nucl. Soc. 83, 294–296.

Takeda, T., Ikeda, H., 1991. 3-D neutron transport benchmarks. J. Nuclear Sci. Technol. 28 (7), 656–669.